Sensors and Actuators A 321 (2021) 112569

Contents lists available at ScienceDirect

Sensors and Actuators A: Physical

journal homepage: www.elsevier.com/locate/sna

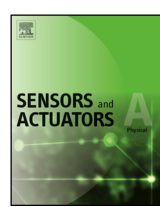

Design and manufacturing of an electrostatic MEMS relay for high power applications

Florian Copt, Yoan Civet*, Christian Koechli, Yves Perriard

Integrated Actuators Laboratory (LAI), École polytechnique fédérale de Lausanne (EPFL), Neuchâtel, Switzerland

ARTICLE INFO

Article history:
Received 7 September 2020
Received in revised form
24 December 2020
Accepted 15 January 2021
Available online 24 January 2021

Keywords:
Contact resistance
Electrostatic
High power
MEMS
Relay

ABSTRACT

This paper addresses the design and manufacturing of a crab-leg based MEMS relay for a high power application. Thanks to a contact resistance lower than 100 mΩ, the relay can hold a current in the order of magnitude of an Ampere without further thermal limitation for the final application. First, an analytical model of the relay, considering its geometry and the contact resistance, is presented. The model is developed in order to focus on the contact deformation. It ensures a low bending moment due to the target contact deformation below 1 nm reducing thus the contact resistance. The design has also been done to overcome the internal resonance frequencies of the future application, i.e. electrical motor. Then, a novel manufacturing process for thicker MEMS is proposed based on micro-fabrication techniques. Finally, the performances of the relay are evaluated and a contact resistance as low as 65 mΩ (comparable to the state-of-the-art) for an applied force of 5 mN, much lower than values reported in the literature is presented.

© 2021 Elsevier B.V. All rights reserved.

1. Introduction

The performance of permanent magnet synchronous motors is defined by their operating range, which is represented by a torque-speed curve. This intrinsic characteristic is defined and fixed by the motors internal and geometrical characteristics and by the power supply. However, motor manufacturers are challenged by customers who require motors with extensive operating ranges. When the electronics is limited, one of the most suitable solutions to increase the operating range is by reconfiguring the winding [1–3]. It resides in a change of the electric connection between the coils. Therefore, commutators are needed.

In the context of switching small power circuits, different components exist such as solid-state and electro-mechanic switches. Solid-state switches can be used but when floating voltages are present, components have to be added in order to guarantee a different voltage between the gate and the source in order to switch it on. Furthermore, since most of these components are not four quadrants, they need to be doubled in order to ensure that the current flows in both directions [4]. This implies that the overall system cannot be easily integrated.

Due to the commercially available relays being too large, the MEMS relays are particularly investigated. Within the MEMS relays, it is possible to differentiate two types: ohmic and capacitive ones. Capacitive relays are frequency switches that work through a variation of their capacitance whereas ohmic ones consist in mechanical on/off switches that drive or stop the connection between two tracks. The latter is thus well suited to our application.

Several MEMS actuation principles exist such as electrostatic, magneto-static, thermal or piezoelectric ones [5]. In our case, electrostatic is chosen because of its low power consumption and fast time response, ease of integration and also considering the magnetic and thermal environment [6] in which the relay will be placed. In terms of energy density the electrostatic relays overcome the magnetic ones when the air gap is smaller than 2 µm [6]. The interest in electrostatically actuated MEMS relay for high power applications have increased these last years [7–13].

The main problem while conceiving an ohmic relay is that its intrinsic resistance is going to produce Joule losses when currents flows through it. Usually, it is more simple to place relays in parallel in order to split the current so that lower current flows through each relay [9]. Indeed, Patel and Rebeiz [7] have shown that it is possible to handle a power higher than 10 W with a current bigger than 1 A despite a contact resistance of 1–2 Ω. Finally, heat is a major factor when it comes to talk about power application [8,10]. It is possible to add a sink insulator [8] or to play with the geometry of

* Corresponding author.
E-mail address: yoan.civet@epfl.ch (Y. Civet).

https://doi.org/10.1016/j.sna.2021.112569
0924-4247/© 2021 Elsevier B.V. All rights reserved.

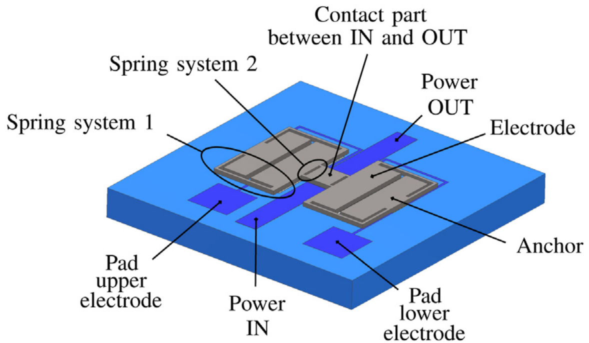

Fig. 1. Proposed relay.

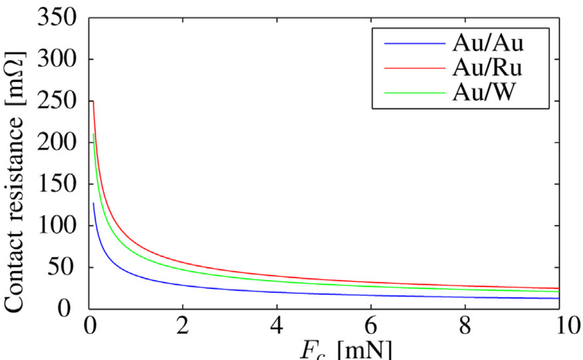

Fig. 2. Contact resistance according to (1) for different materials.

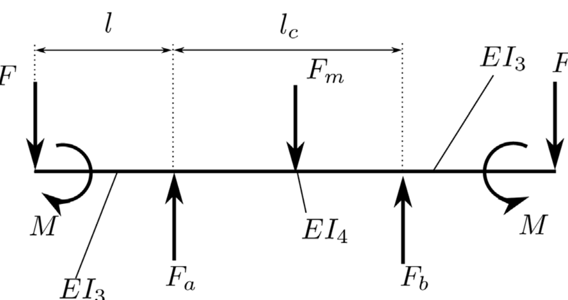

Fig. 3. Schematic of the contact part.

the structure in order to have a heat sink [10] integrated into the relay.

The proposed relay is based on a two-step spring system or crab-leg structure [8] that allows the relay to increase the contact force, while remaining in a 2.5 mm^3 volume constraint for integration purposes in very small motors. Nevertheless, increasing the contact force can add drawbacks. Indeed, the contact can bend due to the applied force around the contact and this will imply a reduction of the quality of the contact. For this reason, the proposed structure integrated a compensation of the contact deformation.

In the paper, an analytical modeling of the relay is undertaken in order to reduce the contact resistance and minimize the bending of the contact. Then, we discuss the manufacturing of such relay. Finally, electromechanical tests are performed to validate the approach.

2. Design and modeling

The relay is presented in Fig. 1 and is composed of four main parts: (i) the spring system 1 which links the anchor and the electrode, (ii) the electrodes for actuation, (iii) the spring system 2, which links the electrode and the contact part, (iv) the contact part. The design is done in four main steps. First of all, the contact resistance for this relay is determined. A particular attention has to be taken for the contact resistance because it is the main resistance of the relay and is responsible of the Joule losses, which we want to avoid or at least reduce.

Then, the geometry of the contact part including the spring system 2 has to be designed followed by the design of the anchor. These two developments correspond to the two-step spring system. Finally, electrodes can be designed. Note that the electrodes and the anchors are considered rigid and resistant to deformation for the analytical model. The fabrication limits are essential and have to be taken into account during the design.

2.1. Contact resistance

The contact resistance depends on three major parameters, i.e. the contact force, the contact area and the harness of the used materials. In a thin gold layer, since the contact radius is bigger than the electron mean free path [14], Maxwell's formula can be used to compute the contact resistance:

$$R_c = \frac{\rho_1 + \rho_2}{4 \cdot a} \tag{1}$$

where ρ_1 and ρ_2 are the resistivity of the respective contact materials and a the effective contact radius expressed as following [15]:

$$a = \sqrt{\frac{F_c}{H \cdot \pi}} \tag{2}$$

with F_c the contact force and H the hardness of the softest of both materials. The contact resistance for different materials is reported in Fig. 2, which shows that the contact force should be at least higher than 2 mN in order to get a low and stable contact resistance.

2.2. Contact part and spring system

When the gap is closing due to the electrostatic force, the electrical contact occurs between the power IN and OUT tracks thanks to the contact structure at first. Then, as the electrostatic force keeps pulling the contact and increases the contact force, the contact may start bending. The contact surface could be drastically reduced. However, it is possible to get rid of this bending moment and improve the contact by modifying the stiffness of the contact. The center part of the system, including the contact structure and the spring system 2, can be modeled as shown in Fig. 3. The electrodes are considered as rigid bodies. F_a and F_b are the reacting forces of the contact, F is the force generated by the electrodes, F_m is the gravity force applied on the contact due to the volume added above it in order to stiffen the structure. By solving the presented system in Fig. 3, using the following boundary conditions:

$$\begin{cases} y1(0) & = y_d \\ y2(\alpha \cdot l + \frac{l}{2}) & = y_c \end{cases} \tag{3}$$

where y_c is the maximum curvature allowed at the center of the contact and y_d the final deflection of the electrode when the power pads are in contact, the deflection at each point of the center part of the relay can be written as follow:

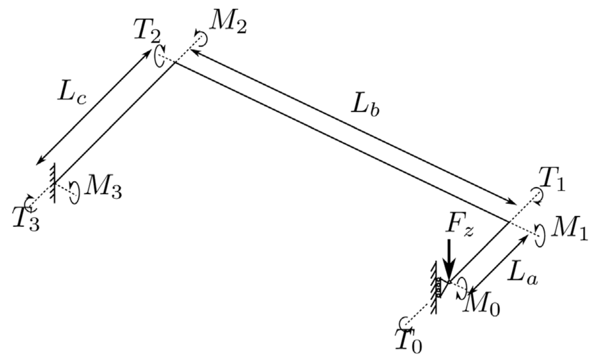

Fig. 4. Body diagram of a relay arm (spring system 1).

$0 < x < l$:

$$y1(x) = \frac{(\alpha \cdot l - x)\left(16 \cdot \alpha^2 EI_4 \cdot F \cdot l^2 + 8 \cdot \alpha \cdot F \cdot l \cdot (3 \cdot EI_3 \cdot l - EI_4 \cdot x) - 3EI_3 \cdot F_m \cdot l^2 - 8 \cdot EI_4 \cdot F \cdot x^2\right)}{48 \cdot EI_3 \cdot EI_4} \quad (4)$$

$l < x < l + \frac{l_c}{2}$:

$$y_2(x) = \frac{(\alpha \cdot l - x)\left(4 \cdot \alpha^2 \cdot l^2 (6 \cdot F + F_m) + 8 \cdot \alpha \cdot l \cdot (3 \cdot F \cdot (l - x) - F_m \cdot x) + F_m \cdot \left(4 \cdot x^2 - 3 \cdot l^2\right)\right)}{48 \cdot EI_4} \quad (5)$$

with

$$\alpha = \frac{l}{l_c} \quad (6)$$

and

$$\beta = \frac{EI_4}{EI_3} \quad (7)$$

where EI_i represents the equivalent flexural rigidity of the part i. The choice of y_c depends on the roughness of the material. For example, gold sputtering gives a peak to peak height of 5 nm [16]. We finally targeted a contact deformation lower than 1 nm in the design to keep a safety margin in regard to the manufacturing process. The parameter y_d has to be chosen considering the geometric limitation and the yield strength of the material used for the arms of the spring system 2.

2.3. Anchor

Here, we focus on the design of the first spring. In order to avoid stiction due to Van der Walls and Casimir forces [17,18], a restoring force F_r of 1 mN might be sufficient. The needed stiffness can be found with (8):

$$k_a = \frac{F_r}{z_1} \quad (8)$$

with k_a the stiffness of the first spring and z_1 the airgap. Considering body diagram of a crab-leg structure (Fig. 4), the stiffness k_a is:

$$k_a = \frac{A}{B + C + D} \quad (9)$$

$$A = 48EGI_1I_2I_3(EI_1I_3L_b + GJ_2(I_3L_a + I_1L_c)) \cdot \quad (10)$$

$$(GI_3J_1L_b + EI_2(I_3L_a + J_1L_c)) \quad (10)$$

$$B = 12E^3 I_1^2 I_2^2 I_3^2 L_a L_b^3 L_c \quad (11)$$

$$+G^3 I_3 J_1 J_2 L_b (I_1 I_3 L_b^3 (I_3 L_a + I_1 L_c)$$

$$+I_2(I_3^2 L_a^4 + I_1^2 L_c^4 \quad (11)$$

$$+2I_1 I_3 L_a L_c (2L_a^2 + 3L_a L_c + 2L_c^2)))$$

$$C = 4E^2 G I_1 I_2 I_3 L_b (I_1 I_3 L_b^3 (I_3 L_a + J_1 L_c) \quad (12)$$

$$+I_2(I_3^2 L_a^4 + I_3 L_a L_c (J_1 L_a^2 + 3J_2 L_a L_b + I_1 L_c^2)$$

$$+I_1 L_c^2 (3J_2 L_a L_b + J_1 L_c^2))) \quad (12)$$

$$D = EG^2 (I_1^2 I_3^3 J_1 L_b^5 + I_2^2 J_2 (I_3 L_a + J_1 L_c) \quad (13)$$

$$\cdot (I_3^2 L_a^4 + I_1^2 L_3^4 + 2I_1 I_3 L_1 L_3 (2L_a^2 + 3L_a L_c + 2L_c^2))$$

$$+4I_1 I_2 I_3 L_b^2 (I_3^2 L_a^2 (J_1 L_a + J_2 L_b) + I_1 J_1 J_2 L_b L_c^2 \quad (14)$$

$$+I_3 L_c (I_1 J_2 L_a L_b + J_1 J_2 L_a L_b + I_1 J_1 L_c^2)))$$

2.4. Electrodes

The electro-statically actuated relay can be synthesized into a spring force due to the stiffness of the beam and the electrodes. Fig. 5 resumes the aforementioned system.

2.4.1. Electrostatic force

The energy of each capacitance C_1 and C_2 is calculated as follows:

$$\begin{cases} W_{e_1} & = \frac{1}{2} \cdot C_1 \cdot U_1^2 \\ W_{e_2} & = \frac{1}{2} \cdot C_2 \cdot U_2^2 \end{cases} \quad (15)$$

with

$$\begin{cases} U_1 = U \cdot \frac{C_2}{C_1 + C_2} \\ U_2 = U \cdot \frac{C_1}{C_1 + C_2} \end{cases} \quad (16)$$

The force between the two surfaces can be calculated by the derivative of the energy in the direction of the motion [19]:

$$\begin{aligned} F_{elec} &= \frac{1}{2} \cdot \frac{\partial C_1}{\partial d_1} \cdot U_1^2 + \frac{1}{2} \cdot \frac{\partial C_2}{\partial d_2} \cdot U_2^2 \\ &= \frac{\varepsilon_0 \cdot A \cdot U^2}{2} \cdot \frac{\varepsilon_{r_1} \cdot \varepsilon_{r_2} \cdot (\varepsilon_{r_1} + \varepsilon_{r_2})}{(\varepsilon_{r_1} z + \varepsilon_{r_2}(z_1 - z))^2} \end{aligned}$$

where ε_0 is the vacuum permittivity, ε_{r_i} is the relative permittivity of each domain i, A is the surface of the electrode and U is the applied voltage on the electrodes.

2.4.2. Pull-in voltage

The point where the electrostatic force and the spring force are equal to each other is called pull-in and occurs in $z_{pull-in}$:

$$z_{pull-in} = \frac{\varepsilon_{r_2} \cdot z_1 + \varepsilon_{r_1} \cdot z_2}{3 \cdot \varepsilon_{r_2}} \quad (17)$$

Consequently, the pull-in voltage is:

$$U_{pull-in} = \sqrt{\frac{8 \cdot k_a \cdot (\varepsilon_{r_1} \cdot d_2 + \varepsilon_{r_2} \cdot d_1)^3}{27 \cdot \varepsilon_0 \cdot (\varepsilon_{r_1} + \varepsilon_{r_2}) \cdot A}} \quad (18)$$

with d_i the thicknesses of the airgap and the oxide respectively.

Using the aforementioned formulae, the final dimensions of the relay satisfying the initial specifications, are presented in Fig. 6 and

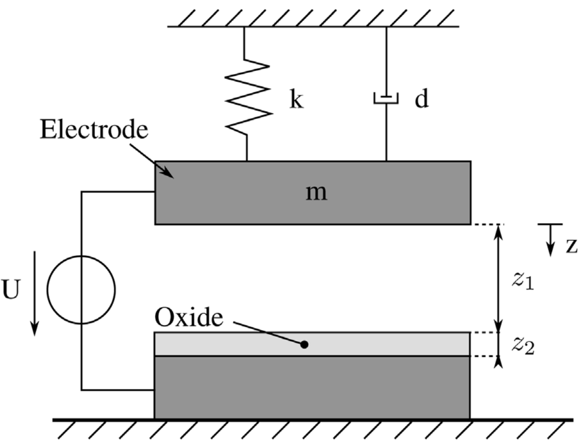

Fig. 5. Simplified electromechanical model of the relay.

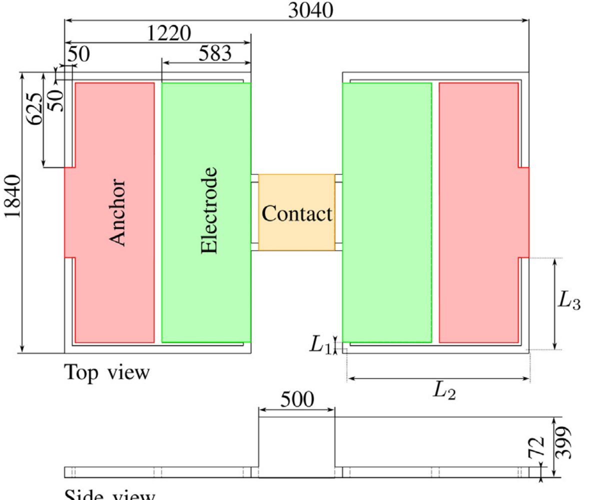

Fig. 6. Dimensions (μm) of the designed relay.

Table 1
Design relay properties.

Parameters	Value	Unit
Contact resistance	168	mΩ
Stiffness	5931	$N.m^{-9}$
Pull-in voltage	190	V
Relay volume	2.23	mm^3

the associated performance is shown in Table 1. The compensation of the contact deformation is obtained thanks to the crab-leg design but also thanks to the thicker cube (500 μm × 500 μm × 277 μm) right in the middle of the contact part.

3. Manufacturing

The literature shows two major tendencies in the manufacturing of MEMS relay: sacrificial layer [20,21] or wafers bonding [22,23]. The former method suffers from stiction and residual defects and often lead to an unsatisfactory process [24]. Among the numerous choices of bonding techniques (direct silicon bonding, anodic bonding, eutectic bonding, glass frit bonding, adhesive bonding), thermocompression [25] combines the advantages of having both mechanical and electrical connections between the two wafers in a single structure and thus, step. The base substrate is a borofloat wafer on which the bottom electrodes, the electrical tracks and the bonding tracks are manufactured. The top wafer is a SOI wafer and is the movable part of the relay. After bonding the two wafers using thermocompression, the backside of the SOI is finally patterned and dry etched in order to release the structures.

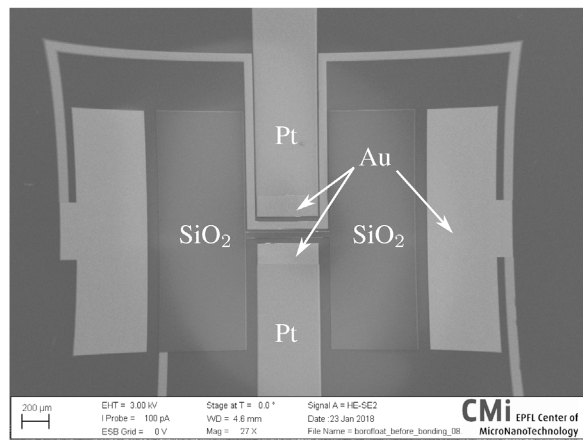

Fig. 7. SEM images at the end of the borofloat wafer process flow. The deformation at the extremities of the structure is due to the limit of the SEM optics.

3.1. Borofloat wafer process

The manufacturing of the first wafer starts (Table 2) with a cleaning performed with a piranha solution which is a mixture of sulfuric acid and hydrogen peroxide (H_2SO_4(96%) + H_2O_2). A thin layer composed of a 20 nm adhesive layer of titanium (Ti), a 500 nm seed layer of gold (Au) and a 20 nm protecting layer of Ti is then deposed (Step 1). This seed layer has three purposes: the creation of the lower electrodes as well as the power track. While the first Ti layer enhances the adhesion to the substrate, the purpose of the Ti layer above the Au is to ensure a good protection of the pads before the electrodeposition. Once the seed layer is sputtered, 8 μm of photoresist is deposed (AZ9221) and patterned. In order to grow 5 μm of gold inside the resist patterned cavities, a ring is left open at the perimeter of the wafer. This is the surface where the current is imposed for the electro-deposition. The exposed titanium inside the patterns and the ring are removed using hydrofluoric acid (HF) in order to get rid of possible resist residues. Finally the electrodeposition is performed. The measured cavity before the electroplating is 8.19 μm (Steps 2 and 3). After the electroplating comes the patterning of the conducting tracks. Firstly, a 8 μm thick photoresist (AZ9260) is deposed and patterned in order to structure the gold by ion beam etching. To prevent from fences, a 2 min reflow at 90 °C on a hot plate smoothes the resist edges profile. The resist is finally stripped (Step 4). Due to contamination restrictions during final backside etching of the SOI, a Ti-Pt lift-off is performed (Step 5). A silicon oxide (SiO_2) layer is sputtered on the wafer with a titanium adhesive layer in order to avoid direct contact between upper and lower electrodes. The thickness of these layers are 200 nm for the SiO_2 and 20 nm for the titanium. The latter is then patterned with a new photolithography step so that the oxide remains only on the electrodes (Step 6). At this point, the addition of the aforementioned oxide layer prevents the electrical signal from being transported between the two power tracks since the electrodes with the oxide layer are higher than the power tracks. In order to solve this problem, a gold lift-off of 500 nm is performed at the contacting part on the power tracks (Step 7, Fig. 7).

3.2. SOI wafer

The proper operation of the relay depends on its stiffness. For this reason, the thickness of the movable part is crucial. A stan-

Table 2
Process flow of the borofloat wafer.

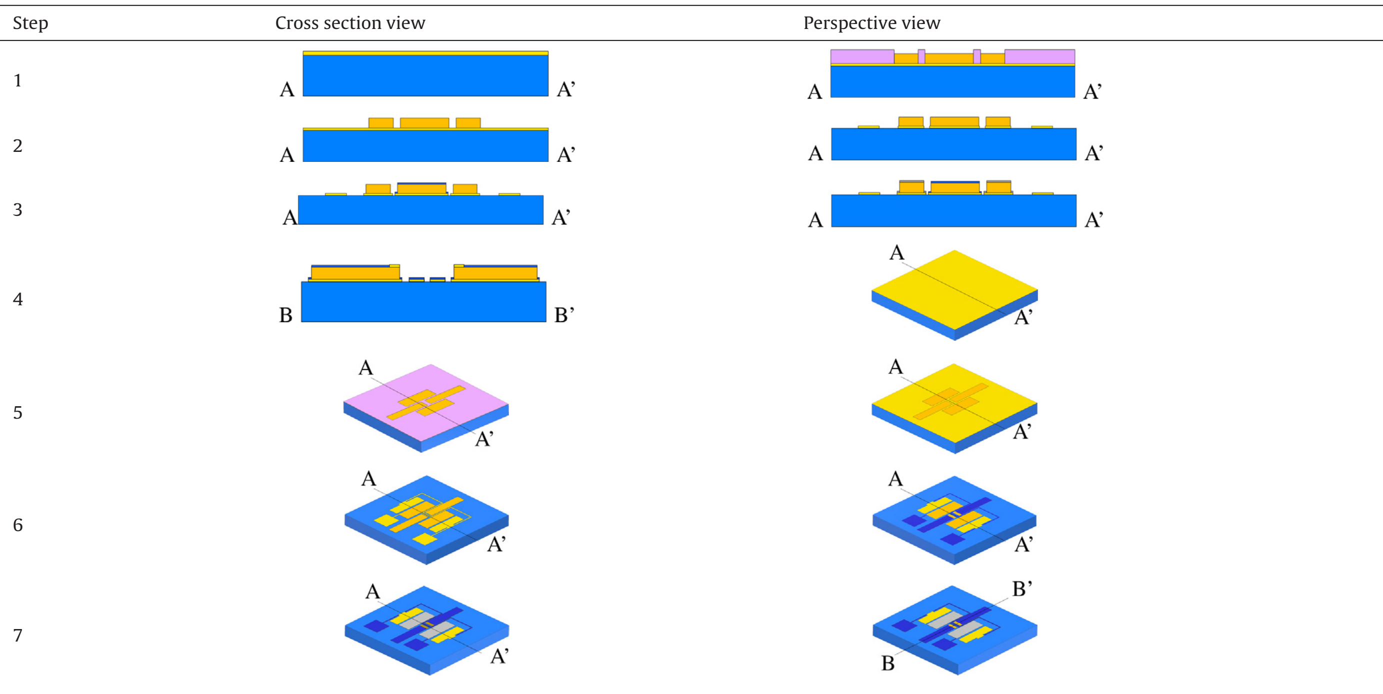

Table 3
Process flow of the SOI wafer.

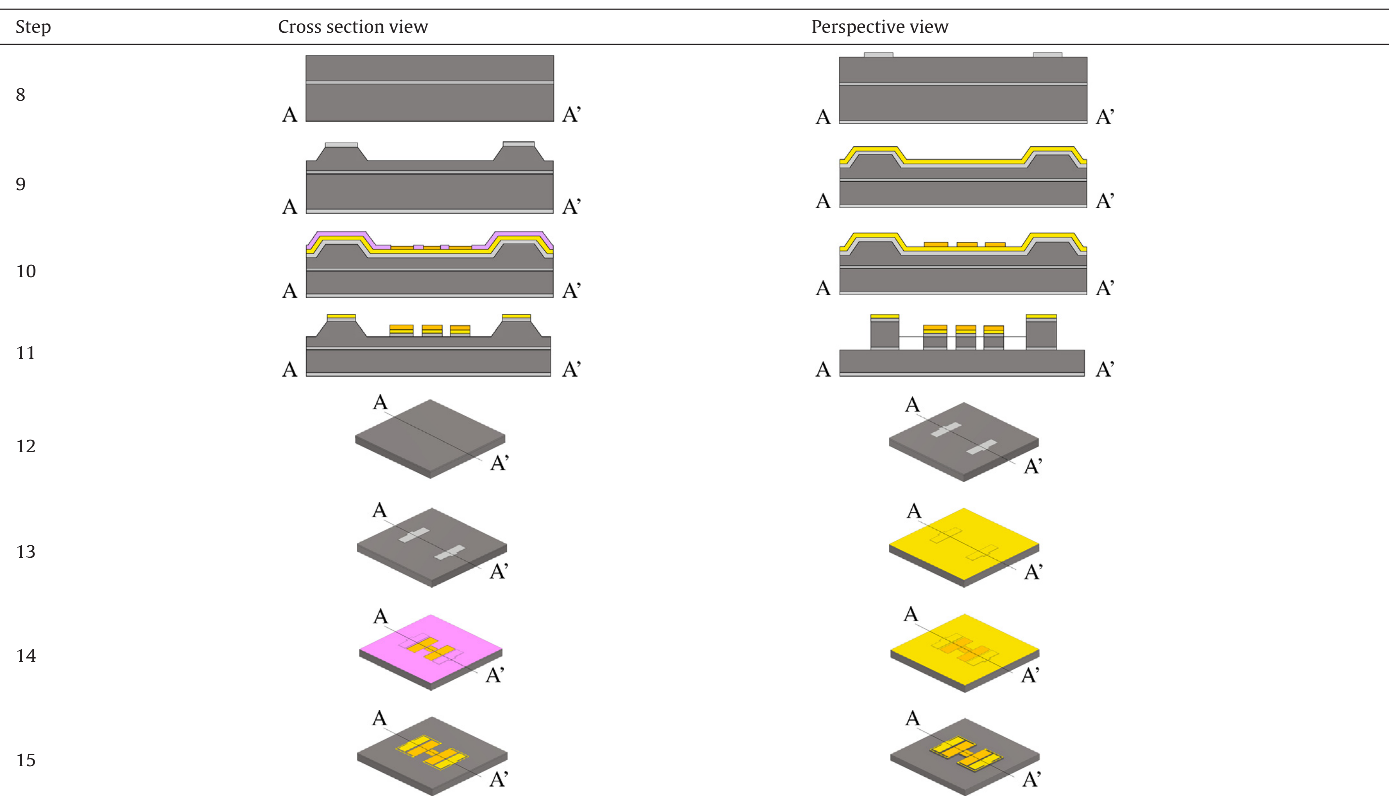

dard SOI wafer (Table 3) is used and thinned thereafter. Firstly, a grinding is used to thoroughly reduce the wafer thickness by 8 μm on the front side and by 48 μm on the back side. To ensure that the roughness caused by the grinding does not affect the bonding [26], a polishing step performed by chemical-mechanical polishing (CMP) is necessary. The latter is 5 μm deep on both sides of the wafer. The surface roughness after the grinding is less than 100 nm with a total thickness variation (TTV) of about 1 μm (Step 8). In order to have the anchor higher than the power track and the electrodes, the top surface of the wafer has to be etched. A wet etch is chosen

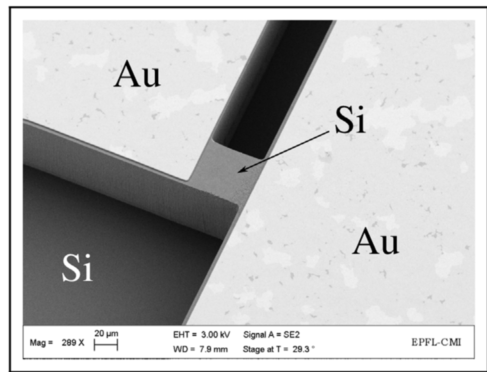

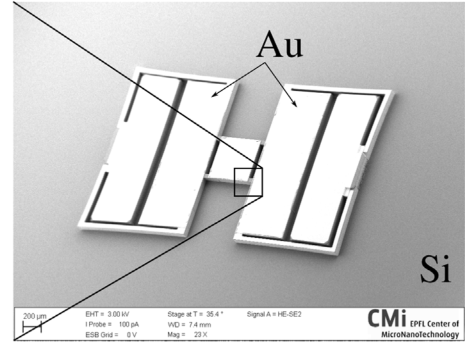

Fig. 8. SEM images at the end of the SOI wafer process flow.

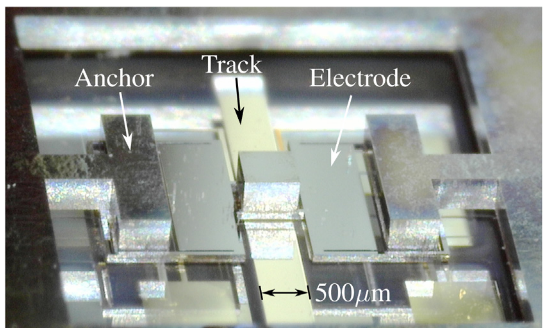

Fig. 9. Optical view of the manufactured relay.

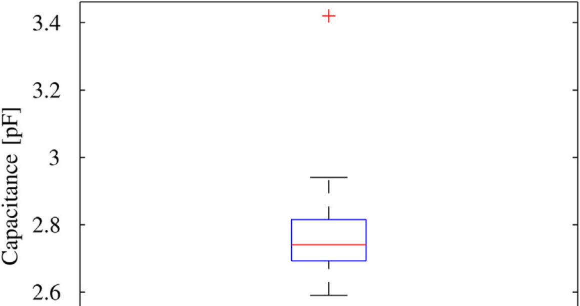

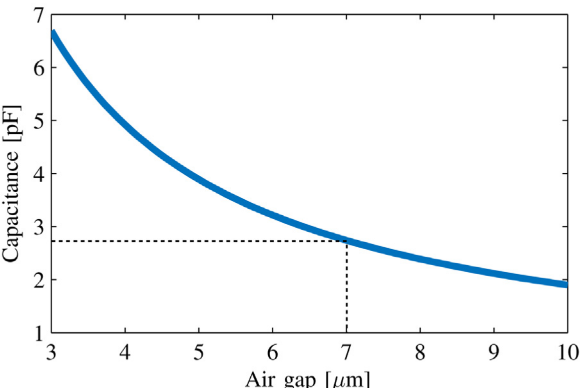

Fig. 10. Capacitance measured on the MEMS relays (upper panel) and variation of the capacitance with 220 nm thick SiO_2 according to the analytical model (lower panel).

to insure electrical connection between upper and lower plateau. The wafer is immersed in a 40% KOH bath at 60 °C (Steps 9 and 10). After removing the potassium residue and SiO_2 hard mask, a new thermal oxidation for electrical insulation is deposed followed by the Ti-Au-Ti seed layer deposition (Step 11). As for the borofloat, 5 µm of gold is grown inside a 15 µm thick cavity of photoresist (Steps 12 and 13). The electric tracks are created by etching the exposed seed layer followed by SiO_2 etching (Step 14). In order to create the movable structure, the top silicon of the SOI is etched on 87 µm and the 2 µm thick buried oxide is removed as well (Step 15, Fig. 8).

3.3. Wafers bonding and release of the relays

Once the two wafers are ready for bonding, a piranha cleaning is performed in order to remove any organic residues and have a high quality bonding surface [26]. After optical alignment, the wafers are bonded at 300 °C with an external applied pressure of 0.15 MPa (Step 16, Table 4). The liberation process of the structure can start by dry etching the SOI backside (Step 17). A silicon oxide dry etch (Step 18) is finally performed to remove any remaining oxide residues due to step 13 and obtain the released relay (Fig. 9).

4. Electromechanical characterization

The functional tests of the relay have been done in four steps: (i) air gap estimation, (ii) stiffness of the structure, (iii) switching measurements, (iv) contact resistance.

4.1. Air gap estimation

Firstly, in order to verify that there is no stiction problem between the two electrodes and estimate the airgap thickness, the capacitance is measured (Fig. 10) using an impedance meter. Starting from Gauss law, the voltage between the two plates is given by integrating the electric field:

$$V = -\int E dl = -\frac{Q}{A \cdot \varepsilon_0}\left(z_1 - z_2 \cdot \left(1 - \frac{1}{\varepsilon_r}\right)\right) \tag{19}$$

The relationship between the capacitance and the airgap is thus deduced:

$$C = \frac{Q}{|V|} = \frac{\varepsilon_0 \cdot A}{z_1 - z_2 \cdot \left(1 - \frac{1}{\varepsilon_r}\right)} \tag{20}$$

where z_1 is the distance between the two electrodes, z_2 is the thickness of the dielectric material, ε_0 is the vacuum permittivity, A is the electrode surface and ε_r is the relative permittivity of the dielectric. Knowing the thickness of the dielectric layer according to measurement during the manufacturing and considering a misalignment of

Table 4
Process flow for the bonding step and the release of the structure.

Step	Cut section view	Perspective view
16		
17		
18		

4%, the estimated airgap is 6.73 μm compare to a value of 7 μm given by the analytical model (Fig. 10).

4.2. Stiffness of the structure

The measurements have been performed using a FemtoTools sensor, which measures forces up to 300 mN with a resolution of 5 μN. The sensor is fixed to a moving plate placed on a Schneeberger^{TM} rail. The linear guidance is done by an endless screw with a pitch of 220 μm, which is fixed to a stepper motor. In order to measure the plate displacement, a laser is used, which reflects on a flat surface fixed on the movable plate. A representation of the system is shown in Fig. 11.

Different stiffness measurements have been performed on the functional prototypes and are shown in Fig. 12. In this figure, as the plate is driven further from the laser, the displacement is negative. As the sensor is delicate, the measurements start when the sensor is 50 μm above the relay. If the sensor would press against a non-flexible silicon bloc, the infinite counter force would be critically damaging. When the sensor touches the relay, the force applied on the sensor increases with the displacement. The slope is the stiffness, which is calculated using a linear regression. Note that the measurements are performed only in the air gap because when the relay is close the stiffness becomes infinite and the force sensor may break.

As a result, the mean value of the measured stiffness is 8019 N . m^{-1}. A 26% error is found between the theoretical stiffness according to the initial design (5931 N . m^{-1}) compared to the previous measured value.

4.3. Switching measurements

During the electrical tests of the MEMS relay, the air gap decreases due to the electrostatic force. This displacement is measured with a laser sensor, which has a resolution of 50 nm. This laser is vertically positioned on the relay and the voltage is applied with two probes placed on the electrode pads. In Fig. 13, the measurements performed on 5 relays are reported and two of them confronted to theoretical pull-in voltage deduced from the stiffness measurement. The shown deflection of the measurements confirms the expected behavior between the electrostatic force and the spring force. However, a maximum error of 22% is found between the theoretical curve deduced from the stiffness measurements and the measured deflection when a voltage is applied to the electrodes. This error can be justified by the approximation of the stiffness measured due to the noise (as shown in Fig. 12) used to project the theoretical value of the deflection. Once the pull-in occurs, an electrical contact is performed and the relay is turned on.

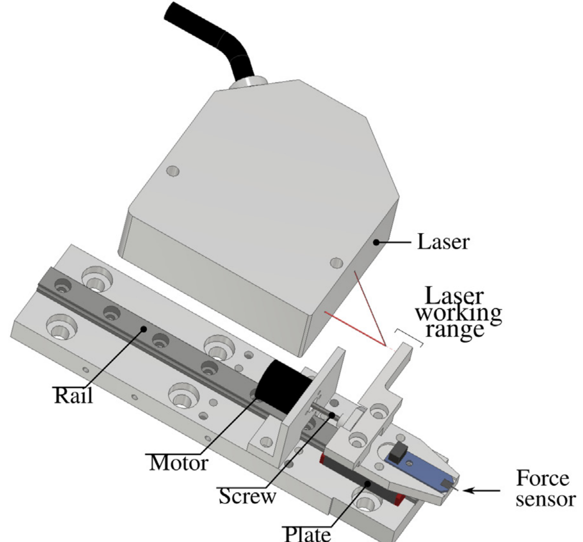

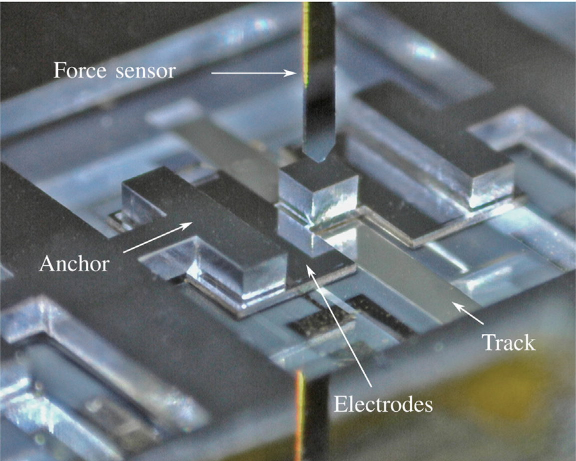

Fig. 11. Schematic view of the custom force-displacement measuring set-up and closer view of the force sensor tip on top of the relay.

4.4. Contact resistance

In order to characterize the contact resistance, the setup presented in Fig. 11 is once again used. The contact resistance is measured through four-point measurements. The results are shown in Fig. 14. The contact resistance is always below 65 mΩ with a contact force of 5 mN. The resistance is thus twice lower than the

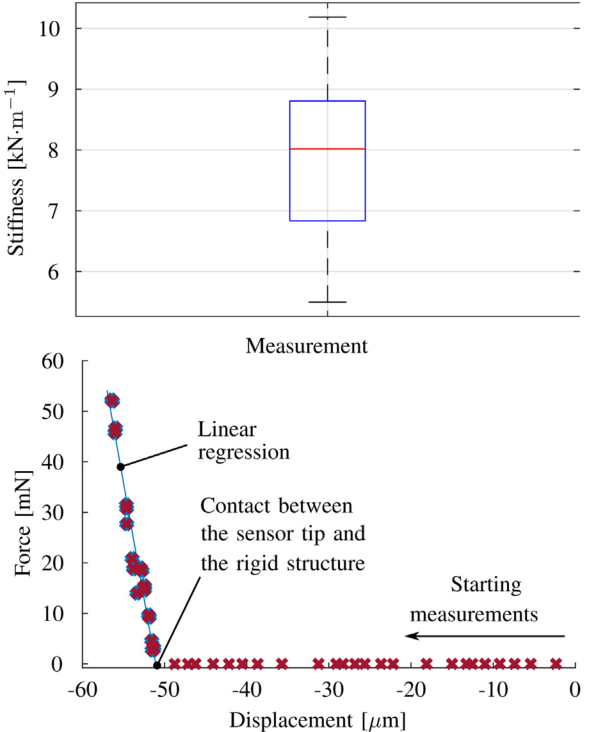

Fig. 12. Stiffness dispersion (upper panel) and force-displacement characteristic of a single relay (lower panel).

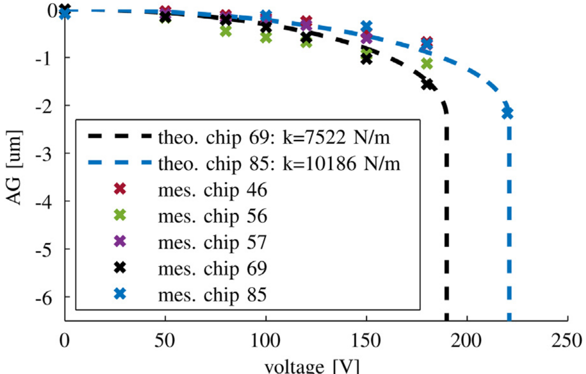

Fig. 13. Deflection of the relay due to an externally applied voltage.

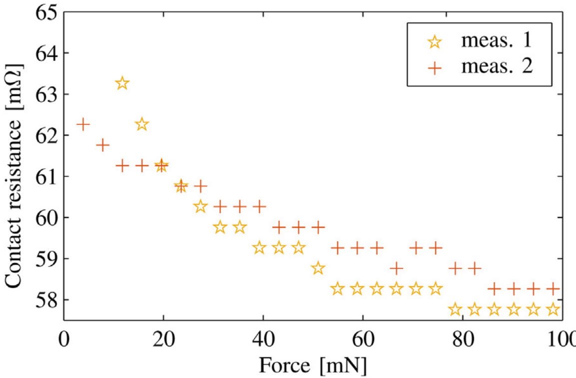

Fig. 14. Contact resistance measurement.

expected value from the analytical model. The analytical model was chosen to be very conservative to make sure that the contact resistance was low enough for the application in the worst case. After deep analysis of the Au metal contact layer, we figured out that the quality of the Au-electroplating steps (2 and 13 in Tables 2 and 3 respectively) were quite poor. Comparing our results to published values in the literature, we have already obtained better performances compared to [12] who has published 13 Ω and we could expect similar results to [8,11] down to a few mΩ with a better gold surface (lower roughness).

5. Conclusion

We have proposed the design of an electrostatic MEMS relay working in harsh environment and presenting a low contact resistance fulfilling the requirement of electromagnetic motor. Since the contact resistance depends on both the contact surface and force, a two-spring (or crab-leg) structure is used. The proposed design also ensures the flatness of the contact to overcome the main disadvantage of such a structure. This relay has been manufactured using standard cleanroom microfabrication techniques. The process flow is composed of 18 main steps combining two initial wafers. The electromechanical tests have validated the design and the new manufacturing procedure with a contact resistance down to 64 mΩ for a 5 mN applied force. It thus confirms the possibility to integrate such MEMS relay inside a permanent synchronous motor and enlarge the operating range of such device. Considering the work already done, several improvements can be suggested. The quite high voltage to trigger the relay can be easily reduced by dropping the top silicon layer thickness down to 72 μm instead of 93 μm, decreasing therefore the global rigidity of the relay, and potentially reaching an actuation voltage of 30 V; a common value for the power supply of an electromagnetic motor. The latter value would be the lowest actuation voltage ever published for such a low contact resistance. Due to the impact of the contact, the latter can degrade with time, finally leading to failure. Replacing gold by tungsten or ruthenium in one of the two power supply lines will give better stability over time and less stiction problems without increasing the contact resistance too much.

Author contributions

F.C., C.K. and Y.P designed the research. Y.P supervised the overall project. F.C. and C.K developed the analytical model. F.C. and Y.C fabricated the MEMS. F.C. and C.K. tested the prototypes Y.C., F.C. and Y.P wrote the manuscript. All authors edited and agree with the manuscript.

Conflict of interest

The authors declare that there is no conflict of interest.

Declaration of Competing Interest

The authors report no declarations of interest.

References

[1] F. Caricchi, F. Crescimbini, F. Mezzetti, E. Santini, Multistage axial-flux PM machine for wheel direct drive, IEEE Trans. Ind. Appl. 32 (4) (1996) 882–888.
[2] E. Nipp, Alternative to field-weakening of surface-mounted permanent-magnet motors for variable-speed drives, in: IAS'95. Conference Record of the 1995 IEEE Industry Applications Conference Thirtieth IAS Annual Meeting, vol. 1, IEEE, 1995, pp. 191–198.
[3] E. Nipp, Permanent Magnet Motor Drives with Switched Stator Windings (PhD thesis), Institutionen fr elkraftteknik, 1999.

[4] R. Nathanael, Nano-Electro-Mechanical (NEM) Relay Devices and Technology for Ultra-Low Energy Digital Integrated Circuits. Technical Report, California Univ Berkeley Dept of Electrical Engineering and Computer Science, 2013.
[5] G.M. Rebeiz, RF MEMS: Theory, Design, and Technology, John Wiley & Sons, 2004.
[6] G. Schiavone, M.P.Y. Desmulliez, A.J. Walton, Integrated magnetic MEMS relays: status of the technology, Micromachines 5 (3) (2014) 622–653.
[7] C.D. Patel, G.M. Rebeiz, A high-reliability high-linearity high-power RF MEMS metal-contact switch for DC40-GHz applications, IEEE Trans. Microw. Theory Tech. 60 (10) (2012) 3096–3112.
[8] Y.-H. Yoon, Y.-H. Song, S.-D. Ko, C.-H. Han, G.-S. Yun, M.-H. Seo, J.-B. Yoon, Highly reliable MEMS relay with two-step spring system and heat sink insulator for power applications, in: 2015 28th IEEE International Conference on Micro Electro Mechanical Systems (MEMS), IEEE, 2015, pp. 114–117.
[9] B. Ma, Z. You, Y. Ruan, S. Chang, G. Zhang, Electrostatically actuated MEMS relay arrays for high-power applications, Microsyst. Technol. 22 (4) (2016) 911–920.
[10] F.M. Ozkeskin, Y.B. Gianchandani, Micromachined Pt–Rh and stainless steel relays for high power DC applications, Sens. Actuators A: Physical 176 (2012) 130–137.
[11] Y.-H. Song, D.-H. Choi, H.-H. Yang, J.-B. Yoon, An extremely low contact-resistance MEMS relay using meshed drain structure and soft insulating layer, J. Microelectromech. Syst. 20 (1) (2011) 204–212.
[12] J. Liu, Z. Shu, C. Wang, H. Shan, P. Yin, F. Zhang, Y. Zhang, Z. Xiong, L. Du, B. Tang, Fabrication of a flexible polyimide-based electrostatically actuated MEMS relay, J. Micromech. Microeng. 28 (10) (2018) 105004.
[13] Y.-H. Yoon, Y. Jin, C.-K. Kim, S. Hong, J.-B. Yoon, 4-Terminal MEMS relay with an extremely low contact resistance employing a novel one-contact design, in: 2017 19th International Conference on Solid-State Sensors, Actuators and Microsystems (Transducers), IEEE, 2017, pp. 906–909.
[14] R. Coratger, C. Girardin, R. Pchou, F. Ajustron, J. Beauvillain, Determination of the electron mean free path in the 11.8 eV energy range in thin gold layers using ballistic electron emission microscopy, Eur. Phys. J. Appl. Phys. 5 (3) (1999) 237–242.
[15] R. Holm, Electric Contacts: Theory and Application, Springer Science & Business Media, 2013.
[16] G.W. Tormoen, J. Drelich, E.R. Beach, Analysis of atomic force microscope pull-off forces for gold surfaces portraying nanoscale roughness and specific chemical functionality, J. Adhes. Sci. Technol. 18 (1) (2004) 1–17.
[17] A. Hariri, J.W. Zu, R. Ben Mrad, Modeling of dry stiction in micro electro-mechanical systems (MEMS), J. Micromech. Microeng. 16 (7) (2006) 1195.
[18] F. Michael Serry, D. Walliser, G.y Jordan Macla, The role of the Casimir effect in the static deflection and stiction of membrane strips in microelectromechanical systems (MEMS), J. Appl. Phys. 84 (5) (1998) 2501–2506.
[19] P.D. Hanasi, B.G. Sheeparamatti, B.B. Kirankumar, Study of pull-in voltage in MEMS actuators, in: 2014 International Conference on Smart Structures and Systems (ICSSS), IEEE, 2014, pp. 108–111.
[20] G. Schiavone, S. Smith, J. Murray, J.G. Terry, M.P.Y. Desmulliez, A.J. Walton, Micromechanical test structures for the characterisation of electroplated NiFe cantilevers and their viability for use in MEMS switching devices, in: 2013 IEEE International Conference on Microelectronic Test Structures (ICMTS), IEEE, 2013, pp. 13–18.
[21] G. Schiavone, A.S. Bunting, M.P.Y. Desmulliez, A.J. Walton, Fabrication of electrodeposited NiFe cantilevers for magnetic MEMS switch applications, J. Microelectromech. Syst. 24 (4) (2014) 870–879.
[22] Y. Gao, Z. You, J. Zhao, Electrostatic comb-drive actuator for MEMS relays/switches with double-tilt comb fingers and tilted parallelogram beams, J. Micromech. Microeng. 25 (4) (2015) 045003.
[23] Y. Komura, M. Sakata, T. Seki, K. Kobayashi, K. Sano, S. Horiike, K. Ozawa, Micro machined relay for high frequency application, Proceedings of the Relay Conference-National Association of Relay Manufacturers, vol. 47 (1999) 12.
[24] N. Tas, T. Sonnenberg, H. Jansen, R. Legtenberg, M. Elwenspoek, Stiction in surface micromachining, J. Micromech. Microeng. 6 (4) (1996) 385.
[25] C.H. Tsau, Fabrication and Characterization of Wafer-Level Gold Thermocompression Bonding (PhD thesis), Massachusetts Institute of Technology, 2003.
[26] J. Fan, C.S. Tan, Y. Pardhi, Low temperature wafer-level metal thermo-compression bonding technology for 3D integration, Metall. Adv. Mater. Process. 52 (2) (2012) 302–311.

Biographies

Florian Copt received the M. Sc. in Microengineering and the Ph.D. from the Swiss Federal Institute of Technology of Lausanne (EPFL) in 2013 and 2018 respectively. He worked as a Postdoctoral Fellow until 2019 at the Integrated Actuator Laboratory of EPFL. His research interests are in permanent magnet motors (mechanical and electronic drives design and control) and microfabrication technologies and their applications.

Yoan Civet graduated from Grenoble Institute of Technology in France, Swiss Federal Institute of Technology – Lausanne (EPFL) in Switzerland and Politechnico di Torino in Italy with a specialty in Micro and Nanotechnologies for Integrated Systems in 2008, received the Ph.D. degree in Nanoelectronics and Nanotechnologies from the Université de Grenoble, France, in 2012 for his thesis on MEMS resonators frequency compensation. In 2013, he joined EPFL as Postdoctoral Fellowship and is now in charge of the Center for Artificial Muscles in Neuchâtel aiming to develop soft actuators for biomedical applications.

Christian Koechli received the M.Sc. and Ph.D. in 1995 and 1999 from the Ecole Polytechnique Fédérale de Lausanne (EPFL), Switzerland, in electrical engineering. He is sharing his time between industrial development at Micro Beam SA in Yverdon, research and teaching at EPFL. His research interests are in the field of electromechanical systems and electric drives.

Yves Perriard Yves Perriard (SM05) is born in Lausanne, Switzerland, in 1965. He received the M.Sc. degree in microengineering and the Ph.D. degree from the Swiss Federal Institute of Technology of Lausanne (EPFL), Lausanne, Switzerland, in 1989 and 1992, respectively. He was a Co-Founder of Micro-Beam SA. In 1998, he joined EPFL as a Senior Lecturer, becoming a Professor in 2003 where he is currently the Director of the Laboratory of Integrated Actuators. His research interests are in the field of new actuator design and associated electronic devices. In 2018, he is granted of 12 million CHF to build up a new Center for Artificial Muscles (CAM) at EPFL. Prof. Perriard is a Member of the Executive Council and the board of the European Power Electronics Association (EPE), Brussels.